

# The interactive bending wrinkling behaviour of inflated beams

Y. P. Liu<sup>1</sup>, C. G. Wang<sup>1,2\*</sup>, H. F. Tan<sup>1,2</sup>, M. K. Wade<sup>3</sup>

<sup>1</sup>*Center for Composite Materials, Harbin Institute of Technology, Harbin, 150001, China*

<sup>2</sup>*National Key Laboratory of Science and Technology on Advanced Composites in Special Environments, Harbin Institute of Technology, Harbin 150080, China.*

<sup>3</sup>*College of Engineering, Mathematics and Physical Sciences, University of Exeter, North Park Road, Exeter, Devon EX4 4QF, United Kingdom.*

## Abstract

A model is proposed based on a Fourier series method to analyse the interactive bending wrinkling behaviour of inflated beams. The whole wrinkling evolution is tracked and divided into three stages by identifying the bifurcations of the equilibrium path. The critical wrinkling and failure moments of inflated beam are then able to be predicted. The global-local interactive buckling pattern is elucidated by the proposed theoretical model and also verified by non-contact experimental tests. The effects of geometric parameters, internal pressure and boundary conditions on the buckling of inflated beams are investigated in the end. Results reveal that the interactive buckling characteristics of inflated beam under bending are more sensitive to the dimensions of the structure and boundary conditions. We find that beams which are simply supported at both ends or clamped and simply supported boundary conditions may prevent the wrinkling formation. The results provide significant support for our

---

\* Corresponding author E-mail: wangcg@hit.edu.cn

understanding of the bending-wrinkling behaviour of inflated beams.

*Keywords:* Inflated beam; Bending wrinkling; Wrinkling evolution; Interactive pattern; Fourier series method

## 1. Introduction

As one of the most typical membrane-like structures, inflated beams have been the subject of interest in recent years owing to their distinctive features. They are of much lower weight and cost, can be folded easily and deployed quickly. Hence, they are widely applied to terrestrial and aerospace structures [1]. However, an inflated beam is a typical thin-wall structure and the instability phenomena, including global buckling, local wrinkling or both, may easily occur [2, 3]. Investigations on the instability phenomena of these structures can be categorized into two categories: global buckling analysis and local wrinkling analysis.

The global buckling, as its name suggests, analysis mainly focuses on a global buckling mode and critical buckling load. Euler-Bernoulli's kinematics was widely adopted because of its simplicity and ability correctly to determine the structural response in many practical situations. Pioneering work was carried by [Comer and Levy](#) [4] who provided analytical expressions for the deflection in an inflated cantilever beam by means of Euler-Bernoulli's kinematics. Then, [Main et al.](#) [5] conducted experiments on cantilever inflated beams and compared the results with [Comer and Levy's](#) theory [4]. [Suhey et al.](#) [6] considered a pressurized tube under uniformly distributed load in ocean aquaculture and theoretical results were obtained assuming Euler-Bernoulli's kinematics as well. However, this theory did not consider

shear and inflation pressure effects on inflated beams. In order to improve the previous formulations, many other authors preferred to use the Timoshenko beam theory which is more appropriate for thin-walled beams. [Fichter \[7\]](#) published a paper in which the internal pressure appears in the deflection expression based on the minimization of total potential energy. By taking into account the deformed state of the beam, [Wielgosz and Thomas \[8, 9\]](#) gave analytical expressions for inflated beams and panels using Timoshenko beam theory. In their approach, the force generated by internal pressure was treated as a follower force which accounted for pressure stiffening effects. [Le van and Wielgosz \[10\]](#) improved [Fichter's \[7\]](#) theory by using the principle of virtual work in the context of the total Lagrangian formulation and proposed solutions for the bending and buckling of an inflated tube. [Davids and Zhang \[11\]](#) developed [Fichter's \[7\]](#) results by considering the pressure work during the volume change in isotropic Timoshenko beams and accounted for fabric wrinkling via a moment-curvature nonlinearity. [Apedo et al. \[12\]](#) developed efficient numerical techniques for predicting the nonlinear load – displacement response of inflated beams by proposing a 3D Timoshenko beam with a homogeneous orthotropic woven fabric. [Barsotti and Ligarò \[13\]](#) assessed the nonlinear elastic response of an inflated cylindrical beam through a simple mechanical model. The geometrical nonlinearities in the model due to both the cross-sectional ovalization and wrinkling were carefully considered.

Distinct from the global buckling analysis, local wrinkling is assumed to occur when the maximum compressive stress reaches the uniform compression critical value

for a circular tube. Three models are used to describe the wrinkling of the inflated beam: the membrane model, the thin-shell model and the shell-membrane model. [Haughton and McKay \[14\]](#) adopted the membrane model to predict the wrinkling characteristics of the inflated beam where the wrinkles occurred when the axial compression reached zero. In the membrane model, both the wrinkling and the collapse moments are independent of the material properties, and are only related to the structural cross-section size and inflation pressure. Then, [Veldman \[15\]](#) regarded the inflated beam as a thin-shell and predicted the wrinkling and collapse moments utilizing the buckling critical load of a shell. In fact, the membrane and thin-shell models correspond to two perfect states respectively which are different from experimental results [\[16-18\]](#). Therefore, [Wang et al. \[18\]](#) proposed a shell-membrane model using a modified factor based on the membrane and thin-shell models. Compared with previous models, the shell-membrane model showed a better correlation with the experimental results in predicting the wrinkling and collapse loads of inflated beams.

Inflatable structures do have additional stiffness which comes from initial pressure, but do not contain the stiffness that comes from material and shape. Both buckling and wrinkling mean a deformation process in which a structure subjected to high compressive stress undergoes a sudden change in morphology at a critical load. When the beam is compressed axially, beyond a certain critical load it spontaneously bows outwards, which is called global or Euler buckling. Compared to global buckling, characteristics of local wrinkling are wavelike and periodic. The above

review of literature indicates that the global buckling analysis focuses on the prediction of global buckling characteristics, such as the critical bifurcation and collapse loads, the wrinkling region and the buckling mode. In contrast, the local wrinkling analysis focuses on the local wrinkling characteristics, such as the wrinkling amplitude, the wrinkling wavelength, the wrinkling number and the wrinkling configuration. Furthermore, most of the experiments on the instability phenomena concentrate on the detection of the global buckling characteristics [19, 20] or of the local wrinkling characteristics [21]. Few papers focus on both of these features in theoretical or experimental studies. Consequently, there is a need to develop theoretical and experimental methods for describing the instability phenomena that couples global and local wrinkling characteristics. A Fourier series method, which corresponds to the periodic and sinusoidal characteristics of wrinkles correctly, is able to account for instability phenomena, such as bending instabilities of circular tubes [22, 23], buckling of sandwich structures [24] or of a Winkler foundation beam [25].

In this paper, the Fourier series method is introduced to the Fichter's [7] theory to derive a Fourier model which can characterize the interactive bending wrinkling behaviour of inflated beams. The non-linear governing equations of the Fourier model are then solved by a Newton trust region method [26]. The whole wrinkling evolution is tracked using the proposed model and the predicted buckling patterns are verified by the non-contact experimental tests. Finally, the effects of geometric parameters, internal pressure and boundary conditions on the buckling of inflated beam are

investigated

## 2. Methodology

### 2.1 Classical model of inflated beam

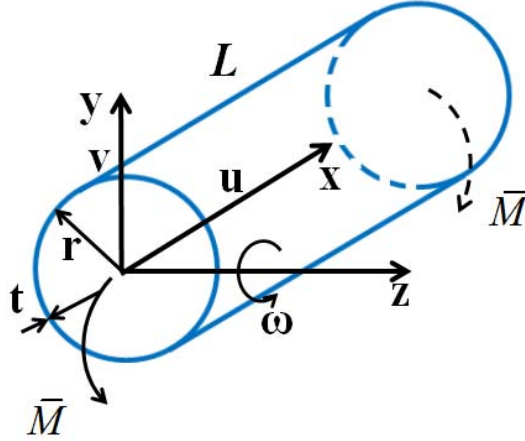


Fig. 1. Schematic representation of the inflated beam, beam, defining axes, dimensions and displacements.

Inflated beams are considered to be thin-walled cylinders which depend on internal pressure for much of their load-carrying ability as shown in Fig. 1. The axial displacement (in the  $x$  direction), transverse displacement (in the  $y$  direction) and rotation angle about the  $z$  axis are represented by  $u$ ,  $v$  and  $\omega$ , respectively. The parameters  $L$ ,  $r$  and  $t$  are respectively the length, cross-sectional radius, and wall thickness of the inflated beam. In-plane means that a steady moment  $\bar{M}$  is applied on each end of the beam about the  $x$ -axis. According to Fichter's [7] theory, a system of equilibrium equations can be obtained from the principle of virtual work following the Timoshenko model:

$$\delta(\Pi_{str} + \Pi_{pres} - \Pi_{ext}) = 0 \quad (1)$$

where  $\Pi_{str}$  and  $\Pi_{ext}$  represent the strain energy and external energy, respectively,

while  $\Pi_{pres}$  represents the potential energy of the internal pressure due to deformation. We make the simplification of neglecting the circumferential strain and twist around the longitudinal axis and thus the strain energy  $\Pi_{str}$  of the inflated beam can be expressed as:

$$\Pi_{str} = \frac{1}{2} \int_0^L (N\varepsilon + Mk + S\gamma) dx \quad (2)$$

where  $\varepsilon$ ,  $\gamma$  and  $k$  are respectively the axial, shearing and bending strain of the inflated beam. Since the inflated beam is made from isotropic Polyurethane thin film, the strains and the corresponding loads ( $N$ ,  $S$ ,  $M$ ) are defined in Eqs. (3)-(4):

$$\begin{aligned} \varepsilon &= u_{,x} + \frac{1}{2} v_{,x}^2 \\ \gamma &= v_{,x} - \omega \\ k &= \omega_{,x} \end{aligned} \quad (3)$$

$$\begin{aligned} N &= 2E\pi r t \varepsilon \\ S &= G\pi r t \gamma \\ M &= E\pi r^3 t k \end{aligned} \quad (4)$$

where  $E$  and  $G$  are the elasticity and shear modulus, respectively. In addition, if the inflated beam is usually made from fabric, Eq. (4) can be replaced by an orthotropic constitutive equation to describe the orthotropic wrinkling behavior in principle. However, in this manuscript, we make the simplification of neglecting the circumferential strain in this Fourier model. Therefore, the expression of orthotropic constitutive equation is almost similar to isotropic Eq. (4). The potential energy  $\Pi_{pres}$  is then given by:

$$\Pi_{pres} = -p\Delta V = -p\pi r^2 \int_0^L \left[ u_{,x} + v_{,x}\omega - \frac{1}{2}\omega^2 \right] dx \quad (5)$$

where  $\Delta V$  is the change in enclosed volume due to deformation,  $p$  is the internal

pressure. In addition, the external work by the applied load  $\Pi_{ext}$  is then given by:

$$\Pi_{ext} = \int_0^L (f_1 u + f_2 v + f_3 \omega) dx + (\bar{N}u + \bar{S}v + \bar{M}\omega) \Big|_0^L \quad (6)$$

where  $f_1$ ,  $f_2$ ,  $f_3$ ,  $\bar{N}$ ,  $\bar{M}$  and  $\bar{S}$  are the external applied loads.

## 2.2 Fourier model of inflated beam

The Fourier series method in this part is adopted to investigate the interactive bending-wrinkling behaviour of the inflated beam. The deformation response of the system is considered as the sum of a slowly-varying mean field and a nearly periodic fluctuation. All the unknowns in Section 2.1 are written in the form of Fourier series:

$$U(x) = \sum_{j=-\infty}^{+\infty} U_j(x) e^{ijqx} \quad (7)$$

where  $U(x)$  is the unknown field which contains functions  $u$ ,  $v$  and  $\omega$ . The Fourier coefficients  $U_j(x)$  represent the envelope for the  $j$ th harmonic, and the coefficients of the zeroth harmonic are real while the others are complex. The frequency  $q$  is defined as  $q = \frac{\pi}{L}n$ , where  $n$  is the wavenumber.

The Fourier coefficients  $U_j(x)$  vary slowly and are assumed to be constant over a period  $[x, x + 2\pi/q]$ . Several calculations have been proposed by [Damil and Potier-Ferry \[27\]](#) to manage the Fourier coefficients. If  $a(x)$  and  $b(x)$  are Fourier series with slowly varying Fourier coefficients as in Eq. (7), the following identities hold:

$$\int_0^L a(x)b(x)dx = \int_0^L \sum_{j=-\infty}^{+\infty} a_j(x)b_{-j}(x)dx \quad (8)$$

$$\left( \frac{da}{dx} \right)_j = (a_{,x})_j = \left( \frac{d}{dx} + \frac{\pi}{L}ijn \right) a_j = a_{j,x} + \frac{\pi}{L}ijna_j \quad (9)$$

$$\left(\frac{d^2 a}{dx^2}\right)_j = (a_{,xx})_j = \left(\frac{d}{dx} + \frac{\pi}{L} i j n\right)^2 a_j = a_{j,xx} + 2\frac{\pi}{L} i j n a_{j,x} - j^2 \left(\frac{\pi}{L} n\right)^2 a_j \quad (10)$$

$$(ab)_j = \sum_{j_1=-\infty}^{+\infty} a_{j_1} b_{j-j_1} \quad (11)$$

By applying the above identities to Eqs. (3)-(4), the force and strain fields of the new Fourier model are obtained as follows:

$$\varepsilon_j = \left(\frac{d}{dx} + \frac{\pi}{L} j i n\right) u_j + \frac{1}{2} \sum_{j_1=-\infty}^{+\infty} \left(\frac{d}{dx} + \frac{\pi}{L} j_1 i n\right) v_{j_1} \left(\frac{d}{dx} + (j-j_1) \frac{\pi}{L} i n\right) v_{j-j_1} \quad (12)$$

$$k_j = \left(\frac{d}{dx} + \frac{\pi}{L} j i n\right) \omega_j \quad (13)$$

$$\gamma_j = \left(\frac{d}{dx} + \frac{\pi}{L} j i n\right) v_j - \omega_j \quad (14)$$

$$N_j = 2E\pi r t \varepsilon_j \quad (15)$$

$$S_j = G\pi r t \gamma_j \quad (16)$$

$$M_j = E\pi r^3 t k_j \quad (17)$$

In the same way, the strain energy and potential energy can be expressed as:

$$\Pi_{str} = \frac{1}{2} \int_0^L \left( \sum_{j=-\infty}^{+\infty} N_j \varepsilon_{-j} + \sum_{j=-\infty}^{+\infty} M_j k_{-j} + \sum_{j=-\infty}^{+\infty} S_j \gamma_{-j} \right) dx \quad (18)$$

$$\Pi_{pres} = -p\pi r^2 \int_0^L \left[ \sum_{j=-\infty}^{+\infty} \left(\frac{d}{dx} + \frac{\pi}{L} i j n\right) u_j + \sum_{j=-\infty}^{+\infty} \left(\frac{d}{dx} + \frac{\pi}{L} i j n\right) v_j \omega_{-j} + \frac{1}{2} \sum_{j=-\infty}^{+\infty} \omega_j \omega_{-j} \right] dx \quad (19)$$

Of course, a more refined picture could be constructed by the inclusion of more Fourier terms, which would also results in a correspondingly more complex and difficult task to ensure numerical convergence. We consider just three envelopes ( $j = -1, 0, 1$ ) as these are sufficient to reveal interactive buckling phenomena.  $U_0$  is identified as the mean value and represents the global deformation, while  $U_1$ , which is conjugated with  $U_{-1}$ , represents the amplitude of fluctuation for the local wrinkling.

Then the energy can be expressed as:

$$\Pi_{str} = \int_0^L [2E\pi r t (\frac{1}{2} \varepsilon_0^2 + |\varepsilon_1|^2) + E\pi r^3 t (\frac{1}{2} k_0^2 + |k_1|^2) + G\pi r t (\frac{1}{2} \gamma_0^2 + |\gamma_1|^2)] dx \quad (20)$$

$$\Pi_{pres} = -p\pi r^2 \int_0^L \left[ u_{0,x} + \left( \frac{d}{dx} + \frac{\pi}{L} in \right) u_1 + \left( \frac{d}{dx} - \frac{\pi}{L} in \right) u_{-1} + v_{0,x} \omega_0 + \left( \frac{d}{dx} + \frac{\pi}{L} in \right) v_1 \omega_{-1} + \left( \frac{d}{dx} - \frac{\pi}{L} in \right) v_{-1} \omega_1 + \frac{1}{2} \omega_0^2 + |\omega_1|^2 \right] dx \quad (21)$$

where the strains in the Fourier model are expressed as:

$$\varepsilon_0 = u_{0,x} + \frac{1}{2} v_{0,x}^2 + v_{1,x}^2 + \left( \frac{\pi}{L} n \right)^2 v_1^2 \quad (22)$$

$$\varepsilon_1 = u_{1,x} + v_{0,x} (v_{1,x} + \frac{\pi}{L} in v_1) \quad (23)$$

$$k_0 = \omega_{0,x} \quad (24)$$

$$k_1 = \left( \frac{d}{dx} + \frac{\pi}{L} in \right) \omega_1 \quad (25)$$

$$\gamma_0 = v_{0,x} - \omega_0 \quad (26)$$

$$\gamma_1 = \left( \frac{d}{dx} + \frac{\pi}{L} in \right) v_1 - \omega_1 \quad (27)$$

As expected, Eqs. (20)-(21) include the mean field  $U_0$  and the amplitude of the fluctuation  $U_1$ , which depicts the interactive instability of the inflated beam. On the other hand, the term  $u_{0,x} + \frac{1}{2} v_{0,x}^2$  in Eq. (22) corresponds to the global strain and the last term  $v_{1,x}^2 + \left( \frac{\pi}{L} n \right)^2 v_1^2$  corresponds to local wrinkling. Meanwhile, the last term is always positive, which implies a decrease of the compressive strain due to local wrinkling. If the beam is in a compressive state, a local instability can occur and these two terms lead to a reduction of compressive stress. Hence, the Fourier model here permits a description of the stress release due to local buckling. Different from the classical expression of strain, the term  $\left( \frac{\pi}{L} n \right)^2 v_1^2$  represents the wrinkling strain which is consistent with the [Calladine's \[28\]](#) results.

In this paper, the wrinkling behaviour of inflated beam is studied under pure bending: moments are applied at both ends of the beam. As there is no applied external axial force and the applied moments are constant, the assumptions  $u(x) = u_0(x)$ ,  $\omega(x) = \omega_0(x)$ , are taken into account, which means the longitudinal displacement and rotation angle do not fluctuate. Here, the research focus is on the interactive global-local instability configuration and not on phase modulation. Therefore, a further approximation is to suppose that the envelope  $v_1(x)$  is real, which only considers amplitude modulation and disregards the evolution of phase. Then, the transverse displacement can be expressed as:

$$v(x) = v_0(x) + 2v_1(x)\cos(qx) \quad (28)$$

By substituting Eqs. (20)-(21) into Eq. (1), the final buckling governing equation of the inflated beam can be deduced as:

$$\varepsilon_{0,x} = 0 \quad (29)$$

$$Et\varepsilon_0 v_{0,xx} + (Et v_{0,x} v_{1,x}^2)_{,x} + \left(Et \left(\frac{\pi}{L}n\right)^2 v_{0,x} v_1^2\right)_{,x} + Gt(v_{0,x} - \omega_0)_{,x} - \frac{1}{2}pr\omega_{0,x} = 0 \quad (30)$$

$$2E\varepsilon_0 v_{1,xx} - 2E\varepsilon_0 \left(\frac{\pi}{L}n\right)^2 v_1 + (E v_{0,x}^2 v_{1,x})_{,x} - E \left(\frac{\pi}{L}n\right)^2 v_{0,x} v_1 + Gv_{1,xx} - G \left(\frac{\pi}{L}n\right)^2 v_1 = 0 \quad (31)$$

$$Er^2 t \omega_{0,xx} + (Gt + pr)(v_{0,x} - \omega_0) = 0 \quad (32)$$

### 2.3 Numerical implementation

The non-linear governing Eqs. (22), (29)-(32) are solved through an incremental Newton-Raphson numerical procedure and enhanced to enable the tracing of post-buckling equilibrium paths through a Newton trust region method [26]. In order to apply this method, the quadratic model  $m$  should be considered at first:

$$\begin{cases} m_k(s) = f(x_k) + g_k^T s + \frac{1}{2} s^T B_k s \\ s.t. \|s\| \leq \delta_k \end{cases} \quad (33)$$

Here,  $g_k$  is the gradient of the objective function  $f(x_k)$  at the current iteration point  $x_k$ .  $s$  is the unknown functions and the step size is required to be bounded by the trust region radius  $\delta_k$ . Both the Cauchy point (the minimizer of  $m$  in the steepest descent direction) and the Newton point are utilized. The incremental step is then given by a combination of the Cauchy step with the Newton step, and the unknowns are determined until the norm of the scaled residual is less than a given tolerance. The computation is started by a damped Newton step. Here, the damping factor, which determines the first Newton step, is set to 0.5 to ensure good convergence. Meanwhile, an initial displacement imperfection is introduced as a geometric imperfection by applying a very small out-of-plane displacement at the center to trigger global buckling. The value of the displacement imperfection is  $10^{-5}$ , and the numerical results show insensitivity to the initial imperfection as long as it is small enough ( $\sim 10^{-5}$ - $10^{-6}$ ), which is also demonstrated by others [17, 29].

### 3. Results and discussions

In this section, we will discuss interactive bending wrinkling behaviour of the simply supported inflated beam under bending without restriction on axial displacement ( $u \neq 0$ ). The interactive buckling characteristics will be obtained by solving the governing Eqs. (22), (29)-(32) which include global deformation ( $v_0$ ) and local wrinkling ( $v_1$ ) using the numerical method in Section 2.3. According to the

following experiments, the material and structural parameters of inflated beam are listed in Table 1.

Tab. 1. Material and geometrical parameters

Parameters	Magnitude
Length of the beam ( $L$ )	$0.3 \pi$ (m)
Young's modulus of beam material ( $E$ )	2.0E8(Pa)
Poisson's ratio ( $\mu$ )	0.3
Radius of the beam ( $r$ )	0.025(m)
Thickness of the beam ( $t$ )	5.0E-5(m)
Internal pressure ( $p$ )	5.0E3(Pa)

### 3.1 Theoretical prediction and experimental verification

The values of moment and deflection values are normalized by  $M_w^s$  and thickness  $t$  respectively, in order to be given in dimensionless terms. Here, the critical wrinkling moment of shell model  $M_w^s$  can be expressed as follows [16, 30]:

$$M_{sw} = p\pi r^3 + \frac{\pi r E t^2}{\sqrt{3(1-\nu^2)}} \quad (34)$$

Then, the dimensionless moment and deflection can be obtained as:

$$m = \bar{M} / M_{sw}, \quad w = v / t \quad (35)$$

Fig. 2(a) illustrates the deformation patterns of the inflated beam under two different applied moments ( $m = 0.37$  and  $0.93$ ). It shows that the structure is unstable when the applied moment is  $0.37$  and global bending deformation dominates the pattern without any local wrinkles. As the applied moment increases to  $0.93$ , local wrinkling is observed and the buckling pattern is the typical interactive buckling between the global bending deformation and local wrinkling. Fig. 2(b) shows a magnified view of the local wrinkles regardless of the global deformation. As seen

from the diagram, local wrinkles distribute along the whole inflated beam and the amplitude of these wrinkles is almost same except for those near the boundary. Wrinkles at the edges are smaller than those in the middle owing to the boundary conditions which restrict on the evolution of local wrinkles.

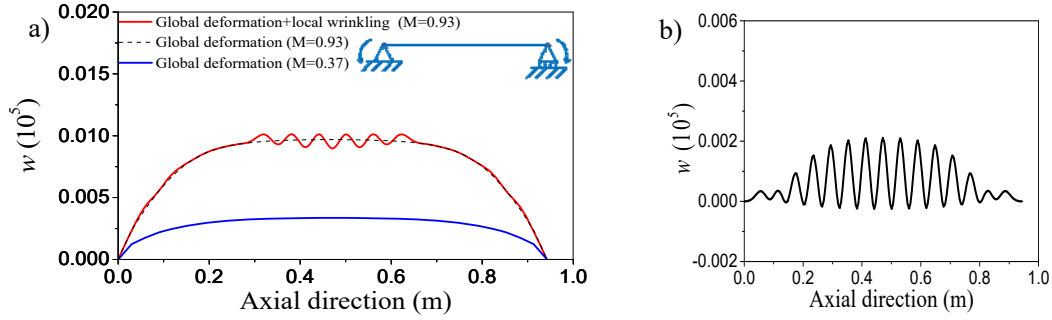


Fig. 2. The deformation patterns of the inflated beam under bending: (a) deformation patterns of the inflated beam under different moments; (b) zoomed view of local wrinkles when the applied moment is 0.93.

In order to verify the theoretical results, a non-contact testing scheme is proposed to measure the buckling pattern of the inflated beam. In the experiment, an inflated beam, which is made from polyurethane thin film, is fixed onto the bending test apparatus (as shown in Fig. 3). The properties of polyurethane thin film are Young's modulus of 200MPa, Poisson's ratio of 0.3 with 50 $\mu$ m thickness. The length and cross-sectional radius are 0.942m and 0.025m, respectively. The bending moment is carried out by rotating a support disk gradually. The buckling pattern is captured using VIC-3D and T-Scan laser tracker instruments (as shown in Fig. 3). The global bending deformation belongs to a macroscale and is captured using VIC-3D instrument based on DIC (Digital Image Correlation) technique which is an effective and reliable method to test the displacement field with an approving precision [31]. There are four

main steps in the VIC-3D wrinkling measurement: (i) random speckles made on the inflated beam surface; (ii) CCD camera calibration; (iii) capture photos; (iv) images post-processing. The local wrinkling configuration belongs to a microscale and is captured using T-Scan laser tracker instrument based on the laser interferometer technique. The instrument can obtain the wrinkling characteristics accurately with a measurement precision of  $1\mu\text{m}$  and a speed of 7000 points per second.

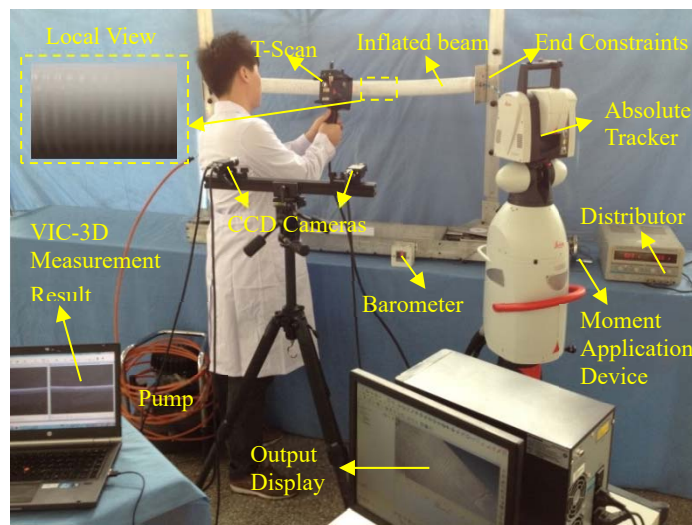


Fig. 3. The wrinkling test apparatus.

The interactive bending wrinkling pattern is observed and tested in the experiment (as shown in Fig. 4). The buckling pattern of the inflated beam under bending behaves as an interactive feature of the global bending deformation and local wrinkling configuration. The experimental results of the global deformation and local wrinkling configuration under  $0.25 \text{ N} \cdot \text{m}$  moment are respectively shown in Fig. 4 (a) and Fig. 4 (b). The tested global deformation ( $0.045\text{m}$ ) agrees with the theoretical result ( $0.041\text{m}$ ) within a difference of 9.7% (as listed in Tab.2). In addition, the ratio of the mean wrinkling amplitude  $A$  to the mean wrinkling wavelength  $\lambda$  is defined as  $\gamma=A/\lambda$  to characterize the local wrinkling level. Large  $\gamma$  ratio changes mean

the high wrinkling level. Obtained from Fig. 4 (b) and Tab.2, the tested ratio  $\gamma$  is 0.23 which is close to the theoretical result (0.20).

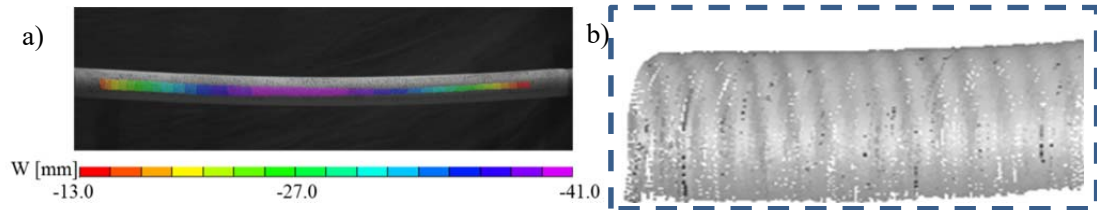


Fig. 4. The experimental interactive bending wrinkling pattern: (a) the experimental global deformation result using VIC-3D instrument; (b) the experimental local wrinkling configuration result using T-Scan laser tracker instrument.

In addition, the global deformations and the ratio  $\gamma=A/\lambda$  (denoting the wrinkling level) under different applied moments are tested and compared with theoretical predictions in Tab.2. Accompanied by the increasing moment, the ratio  $\gamma$  is increased, indicating the rise in the wrinkling level. The tested global deformations are close to the theoretical results within a mean difference of 9.9%. The difference between the experimental and theoretical results may be because the Fourier model is established on a natural state rather than the deformed configuration and the effects of the follower loads are neglected. Moreover, some inevitable limitations in test techniques may also cause the differences between the experiment and theory.

Tab. 2. The experimental and theoretical results of global deformations and  $A/\lambda$

		Applied moment ( N · m )	0.10	0.15	0.25	0.30
Deformation (m)	theoretical results		0.017	0.025	0.045	0.054
	experimental results		0.015	0.023	0.041	0.050
$A/\lambda$	theoretical results		0	0	0.20	0.25
	experimental results		0	0	0.23	0.30

### 3.2 Wrinkling evolution analysis

Fig. 5 shows the moment-deflection response of the inflated beam under bending.

Observed from Fig. 5, there are two critical points which are named as the critical wrinkling point (marked as A) and the failure point (marked as C). The critical wrinkling load corresponds to the point where a nonlinear equilibrium path departs from the initial linear one. The failure point is determined as the following intersection between the bifurcation path and the primary path. Based on the critical points in the equilibrium path, the wrinkling evolution can be divided into three stages, which are named as I, II, III. Stage I (OA) is named as a pre-buckling stage and a linear response characterizes the primary path. In this stage, without any local wrinkles ( $v_1 \rightarrow 0$ ), global bending dominates the deformation pattern of the inflated beam. The applied moment at the critical wrinkling point A is 0.78, which is at the critical wrinkling moment  $M_w$ . When the applied moment reaches  $M_w$ , an obvious bifurcation occurs at the point A and the primary path turns to the bifurcation path. Then the wrinkling evolution goes into Stage II which is identified as the post-buckling stage. The wrinkling strain (the last term in Eq. (22)), which has an abrupt increase due to the local wrinkling formation, is adopted to reflect the first bifurcation. The local wrinkling phenomenon appears in this stage and the pattern characterizes as a typical interactive buckling between the global deformation and local wrinkling. Note that the applied moment has slight effects on the structural deflection in the initial postwrinkling stage (AB). From the view of the energy equilibrium (Eq. (1)), the wrinkling strain energy offsets the increase of external energy. Therefore, in this stage, the wrinkles grow in a relatively stable state and the global bending deformation remains almost stable. In response to the increasing

applied moment, the global deformation and local wrinkling increases simultaneously, which results in a continued monotonic increase in the moment-deflection curve (BC).

When the moment exceeds the failure point C (the failure moment  $M_f = 1.19$ ), the wrinkles eventually localize and cause catastrophic failure in the form of sharp local kinks (as shown in Fig. 5) which promotes the wrinkling evolution into the failure stage (CD). Recall that the results of the Fourier model are obtained under the assumption that the wrinkling configuration has a slow and nearly periodic fluctuation. Thus, the assumption is invalid in the last stage due to the existence of sharp local kinks.

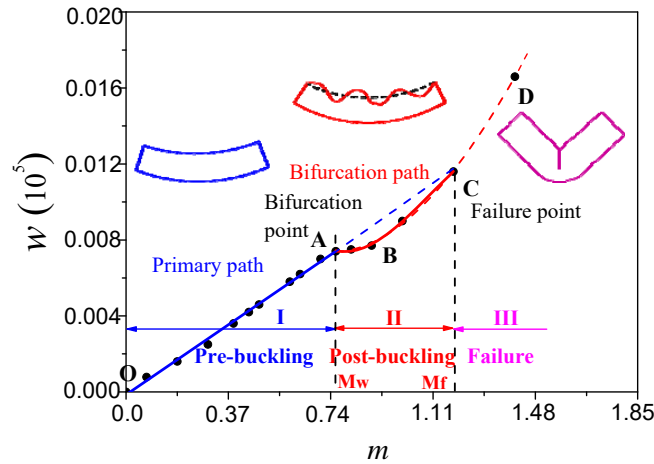


Fig. 5. The numerical moment-deflection response of the inflated beam under bending.

### 3.3 Critical wrinkling moment and failure moment

In this part, the predicted critical wrinkling and failure moments are compared with the results from previous models, including the membrane model [14], the thin-shell model [15] and the shell-membrane model [18]. The comparisons (in Fig. 6) show that the critical wrinkling (0.78) and failure moments (1.19) lie among the results predicted by the shell and membrane models.

In the Fourier model, the structural failure corresponds to the occurrence of sharp local kinks before the wrinkles distribute around the whole cross-section of the inflated beam. However, in the membrane and thin-shell models, the structure fails when the wrinkling angle reaches  $2\pi$  (the whole hoop wrinkles) which does not comply with the practical case. Different from the membrane and thin-shell models, the failure of the shell-membrane inflated beam occurs when the wrinkling angle approaches  $1.5\pi$ , which shows a better correlation with the experimental results and the Fourier model.

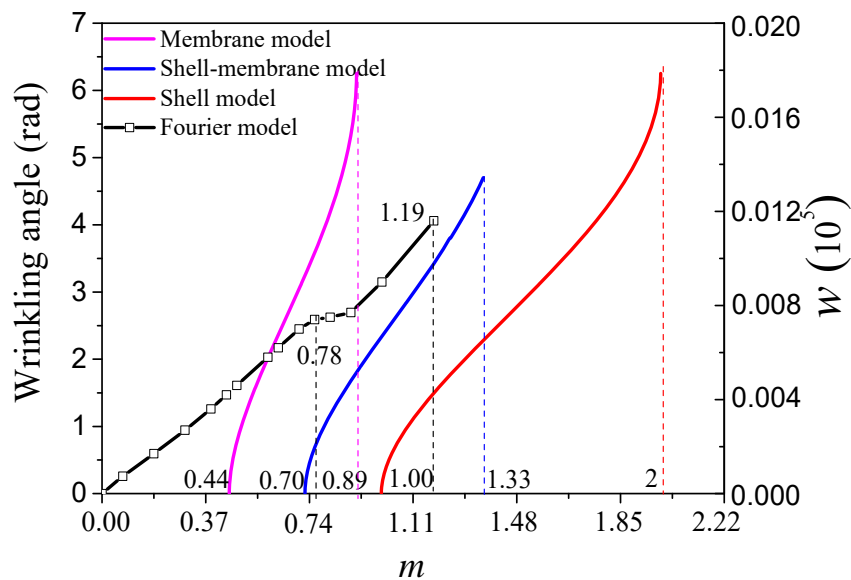


Fig. 6. The numerical critical wrinkling and failure moments from different models.

### 3.4 Internal pressure and structural size

The effects of the internal pressure and structural size on the wrinkling behavior are carried out and shown in Fig. 7. The moment-deflection responses of the inflated beam with 0.025m radius for different internal pressures are shown in Fig. 7 (a). The increasing pressure results in a slight reduction of the deflection and a slight increase

of the critical wrinkling and failure moment. Specifically, for a 40% variation on the assumed pressure of 5kPa, the critical wrinkling moment changes only by 9.52% and the failure moment by 6.45%. It also shows that the critical wrinkling and failure moments are proportional to the internal pressure due to the improvement of the transverse shear stiffness, which is described by Eq. (32). This is in line with the conclusions in the literature [8].

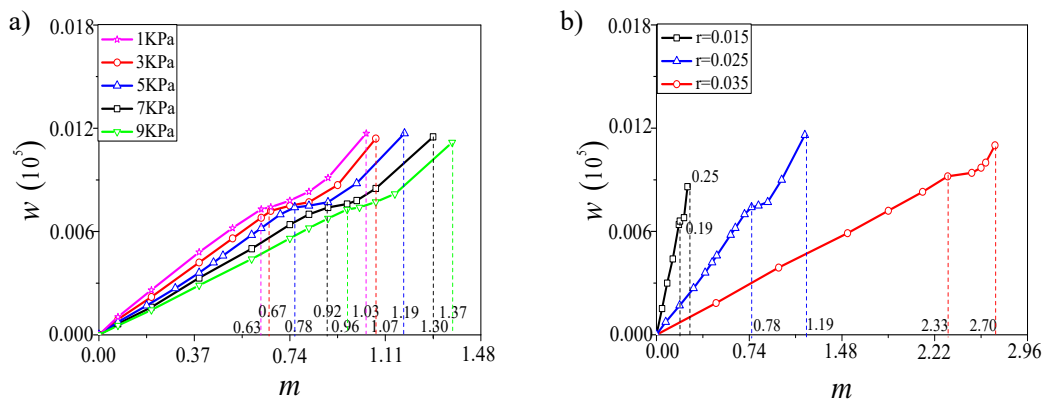


Fig. 7. The numerical moment-deflection responses of the inflated beam with different internal pressures and radii: (a) the moment-deflection responses with different internal pressures; (b) the moment-deflection responses with different radiuses.

Fig. 7 (b) depicts the moment-deflection responses of the inflated beam with internal pressure of 5kPa for different radii (0.015m, 0.025m and 0.035m). An increasing radius results in a large reduction of the deflection and an obvious increase of the critical wrinkling and failure moment due to the improvement of structural stiffness. Specifically, the critical wrinkling and failure moments have a more than three times improvement for a 40% increase on the assumed 0.025m radius. The effects of radius on the critical wrinkling and failure moments are more significant compared with the cases of internal pressure. In addition, for a slender inflated beam,

the sharp local kinks appear quickly after bifurcation due to a slower bending stiffness and a rapid wrinkling evolution. In such cases the inflated beam rapidly fail soon after it is wrinkled.

### 3.5 Boundary conditions

Fig. 8 shows the buckling patterns with the same applied moment ( $0.25 \text{ N} \cdot \text{m}$ ) under four cases with different boundary conditions: simply supported and sliding simply supported (S-SL), simply supported and simply supported (S-S), clamped and sliding simply supported (C-SL), clamped and simply supported (C-S) (note that we refer to sliding which is sometimes elsewhere referred to as rolling). The results in Fig. 8 reveal that the buckling pattern of the inflated beam under bending is closely relevant to the boundary condition. The symmetrical boundary conditions lead to a symmetrical buckling pattern and the same situation is met for nonsymmetrical boundaries.

Global deformation dominates the configuration under the S-S or C-S boundary conditions and there is no wrinkle in these two cases. The configuration under the S-SL or C-SL boundary condition behaves with a typical interactive pattern between the global bending and local wrinkling. Compared with the other two boundary conditions (S-S and C-S), the S-SL and C-SL boundary conditions have no restrictions on the axial displacement ( $u \neq 0$ ) and allow the material to shrink along the axial direction, which leads to an increase of wrinkling strain (the last term in Eq. (22)).

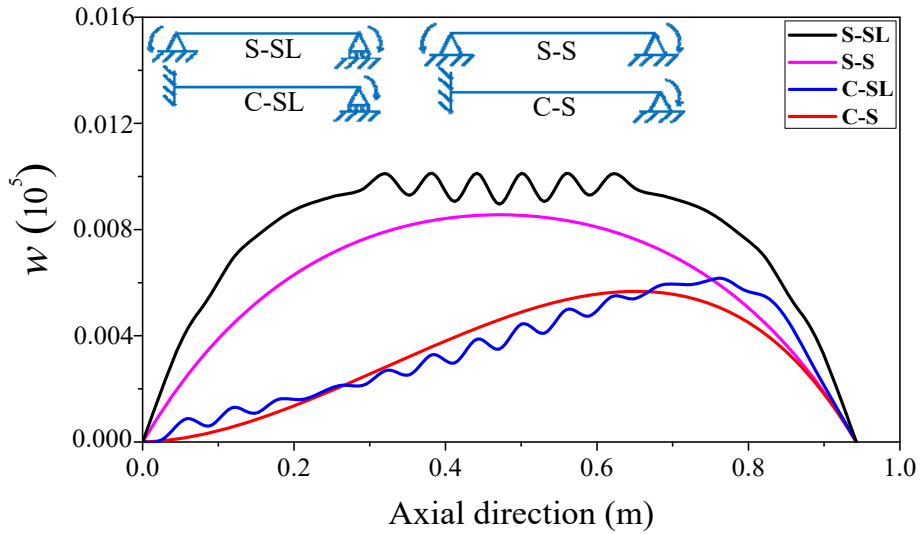


Fig. 8. The buckling patterns under different boundary conditions predicted by Fourier model ( $M = 0.93$ ).

## Conclusions

In this study, the Fourier series method is introduced to the Fichter's theory to derive a Fourier model which can characterize the interactive bending wrinkling behaviour of inflated beams. The whole wrinkling evolution can be tracked using the proposed model and the predicted buckling patterns are verified by the experimental tests. The bending wrinkling behaviour of the inflated beam is closely related to its internal pressure, relative dimensions and boundary conditions. Several important conclusions are drawn as follows.

The wrinkling evolution can be divided into three stages based on the critical wrinkling point and the failure point in the equilibrium path. In the pre-buckling stage, global bending dominates the deformation pattern of the inflated beam without any local wrinkles and a linear response characterizes the primary path. In the post-buckling stage, the local wrinkling phenomenon appears and the pattern

characterizes as a typical interactive buckling between the global deformation and local wrinkling. Finally, the formation of sharp local kinks transforms the wrinkling pattern into the failure stage and accelerates the collapse of the structure.

In the Fourier model, the predicted critical and failure moments are respectively 0.78 and 1.19 and the failure wrinkling angle is amount to  $1.52\pi$ . Moreover, the effects of radius on the critical wrinkling and failure moments are more significant than that of internal pressure. The buckling pattern is quite sensitive to the boundary condition. A larger radius and internal pressure of the inflated beam with an S-S or C-S boundary condition will be a desired consideration to control wrinkling characteristics and evolution. In addition, the inflated beam is made from isotropic polyurethane thin film in the experiment. Therefore, the isotropic constitute equation is adopted here and the orthotropic mechanical behavior of inflated beam made from fabric will be focused on investigation in the future.

### **Data accessibility**

This work has no accompanying data.

### **Authors' contributions**

Y.L. conceived the mathematical models, performed the experimental measurements and drafted the paper. C.W. proposed the idea of the study, funded and supervised the project. H.T. and M.K.W. revised the draft. All authors regularly discussed the progress during the entire work.

## **Competing interests**

We declare we have no competing interests.

## **Ethics**

This work does not pose ethical issues.

## **Funding**

This work is supported by National Natural Science Foundation of China, 11172079 and 11572099; Program for New Century Excellent Talents in University, NCET-11-0807; Natural Science Foundation of Heilongjiang Province of China, A2015002; the Fundamental Research Funds for the Central Universities, HIT.BRETHL.201209 and HIT.MKSTISP.2016 29.

## **Acknowledgement**

The support from NSF is gratefully acknowledged. The authors also would like to thank four anonymous reviewers for their encouragement and helpful comments on an earlier version of the paper.

## **Reference**

1. Jenkins, C.H.M., 2001. Gossamer Spacecraft: Membrane and Inflatable Structures Technology for Space Applications, vol. 191. American Institute of Aeronautics and Astronautics, Reston, Virginia.
2. Jiao, R., Kyriakides, S., 2011. Ratcheting and wrinkling of tubes due to axial

- cycling under internal pressure: Part I experiments. *Int. J. Solids Struct.* 48, 2814-2826.
3. Nguyen, T. T., Ronel, S., Massenzio, M., Jacquelin, E., Apedo, K. L., Phan-Dinh, H., 2013. Numerical buckling analysis of an inflatable beam made of orthotropic technical textiles. *Thin-Wall Struct.* 72, 61-75.
  4. Comer, R. L., Levy, S., 1963. Deflections of an inflated circular cylindrical cantilever beam. *AIAA J.* 1 (7), 1652-1655.
  5. Main, A., Peterson, S. W., Strauss, A. M., 1994. Load-deflection behaviour of space-based inflatable fabric beams. *J. Aerospace Eng.* 2 (7), 225-238.
  6. Suhey, J. D., Kim, N. H., Niezrecki, C., 2005. Numerical modeling and design of inflatable structures-application to open-ocean-aquaculture cages. *Aquacult. Eng.* 33 (4), 285-303.
  7. Fichter, W. B., 1966. A theory for inflated thin wall cylindrical beams. Technical Report, NASA Technical Note, NASA TND-3466.
  8. Wielgosz, C., Thomas, J. C., 2002. Deflection of inflatable fabric panels at high pressure. *Thin-Wall Struct.* 40, 523-536.
  9. Thomas, J. C., Wielgosz, C., 2004. Deflections of highly inflated fabric tubes. *Thin-Wall Struct.* 42, 1049-1066.
  10. Le Van, A., Wielgosz, C., 2005. Bending and buckling of inflatable beams: some new theoretical results. *Thin-Walled Struct.* 43, 1166-1187.
  11. Davids, W. G., Zhang, H., 2008. Beam finite element for nonlinear analysis of pressurized fabric beam-columns. *Eng. Struct.* 30, 1969-1980.

12. Apedo, K. L., Ronel, S., Jacquelin, E., Bennani, A., Massenzio, M., 2010. Nonlinear finite element analysis of inflatable beams made from orthotropic woven fabric. *Int. J. Solids Struct.* 47 (16), 2017-2033.
13. Barsotti, R., Ligarò, S. S., 2014. Numerical analysis of partly wrinkled cylindrical inflated beams under bending and shear. *Thin-Wall Struct.* 84, 204-213.
14. Haughton, D. M., McKay, B. A., 1996. Wrinkling of Inflated Elastic Cylindrical Membrane under Flexure. *Int. J. Eng. Sci.* 34 (13), 1531-1550.
15. Veldman, S. L., 2006. Wrinkling Prediction of Cylindrical and Conical Inflated Cantilever Beams under Torsion and Bending. *Thin-Wall Struct.* 44, 211-215.
16. Veldman, S. L., Bergsma, O.K., Beukers, A., 2005. Bending of anisotropic inflated cylindrical beams. *Thin-Wall Struct.* 43 (3), 461-475.
17. Wang, C. G., Tan, H. F., Du, X. W., Wan, Z. M., 2007. Wrinkling Prediction of Rectangular Shell-Membrane under Transverse In-Plane Displacement. *Int. J. Solids Struct.* 44 (20), 6507-6516.
18. Wang, C. G., Tan, H. F., Du, X. W., He, X. D., 2010. A new model for wrinkling and collapse analysis of membrane. *Acta Mech. Sin.* 26, 617-623.
19. Bardi, F.C., Kyriakides, S., 2006. Plastic buckling of circular tubes under axial compression-part I: Experiments. *Int. J. Mech. Sci.* 48, 830-841.
20. Brayley, K. E., Davids, W. G., Clapp, J. D., 2012. Bending response of externally reinforced, inflated, braided fabric arches and beams. *Constr. Build. Mater.* 30, 50-58.
21. Wong, Y. W., Pellegrino, S., 2006. Wrinkled membranes-Part 1: experiments. *J.*

- Mech. Mater. Struct. 1, 3-25.
22. Karamanos, S. A., 2002. Bending instabilities of elastic tubes. *Int. J. Solids Struct.* 39, 2059-2085.
  23. Houliara, S., Karamanos, A., 2010. Stability of long transversely-isotropic elastic cylindrical shells under bending. *Int. J. Solids Struct.* 47, 10-24.
  24. Léotoing, L., Drapier, S., Vautrin, A., 2002. Nonlinear interaction of geometrical and material properties in sandwich beam instabilities. *Int. J. Solids Struct.* 39, 3717-3739.
  25. Damil, N., Potier-Ferry, M., 2010. Influence of local wrinkling on membrane behaviour: a new approach by the technique of slowly variable Fourier coefficients. *J. Mech. Phys. Solids* 58, 1139-1153.
  26. Dennis, Jr. J. E., Schnabel, R. B., 1996. Numerical methods for unconstrained optimization and nonlinear equations. Vol. 16, Siam.
  27. Damil, N., Potier-Ferry, M., 2006. A generalized continuum approach to describe instability pattern formation by a multiple scale analysis. *Compt. Rendus. Mec.* 334, 674-678.
  28. Calladine, C. R., 1983. *Theory of Shell Structures*. Cambridge University Press. Cambridge.
  29. Wadee, M. A. 2000. Effects of periodic and localized imperfections on struts on nonlinear foundations and compression sandwich panels. *Int. J. Solid Struct.*, 37(8), 1191-1209.
  30. Anonymous. 1965. Buckling of thin-walled circular cylinders, NASA space

vehicle design criteria, NASA SP-8007.

31. Wang, C. G., Lan, L., Tan, H. F., 2013. Secondary Wrinkling Analysis of Rectangular Membrane under Shearing. *Int. J. Mech. Sci.* 75, 299-304.

## Figure and table captions

### Data Statement

No additional unpublished data are available.

Tab. 1. Material and geometrical parameters

Tab. 2. The experimental and theoretical results of global deformations and  $A / \lambda$

Fig. 1. Schematic representation of the inflated beam, beam, defining axes, dimensions and displacements.

Fig. 2. The deformation patterns of the inflated beam under bending: (a) deformation patterns of the inflated beam under different moments; (b) zoomed view of local wrinkles when the applied moment is 0.93.

Fig. 3. The wrinkling test apparatus.

Fig. 4. The experimental interactive bending wrinkling pattern: (a) the experimental global deformation result using VIC-3D instrument; (b) the experimental local wrinkling configuration result using T-Scan laser tracker instrument.

Fig. 5. The numerical moment-deflection response of the inflated beam under bending.

Fig. 6. The numerical critical wrinkling and failure moments from different models.

Fig. 7. The numerical moment-deflection responses of the inflated beam with different internal pressures and radii: (a) the moment-deflection responses with different internal pressures; (b) the moment-deflection responses with different radiuses.

Fig. 8. The buckling patterns under different boundary conditions predicted by Fourier model ( $M = 0.93$ ).